Estimating the recharge properties of the deep ocean using noble gases and helium isotopes

Brice Loose[1], William J. Jenkins[2], Roisin Moriarty[3], Peter Brown[4], Loic Jullion[5], Alberto C. Naveira Garabato[6], Sinhue Torres Valdes[4], Mario Hoppema[7], Chris Ballentine[8], and Michael P. Meredith[9]

[1]Graduate School of Oceanography, University of Rhode Island, Narragansett, Rhode Island, USA, [2]Woods Hole Oceanographic Institution, Marine Chemistry and Geochemistry, Woods Hole, Massachusetts, USA, [3]University of East Anglia, Norwich, UK, [4]National Oceanography Centre, Southampton, UK, [5]Aix-Marseille Université, Institut Méditerranéen d'Océanographie, Marseille, France, [6]National Oceanography Centre, University of Southampton, Southampton, UK, [7]Alfred Wegener Institute Helmholtz Centre for Polar and Marine Research, Climate Sciences, Bremerhaven, Germany, [8]Department of Earth Sciences, University of Oxford, Oxford, UK, [9]British Antarctic Survey, Cambridge, UK

Abstract The distribution of noble gases and helium isotopes in the dense shelf waters of Antarctica reflects the boundary conditions near the ocean surface: air-sea exchange, sea ice formation, and subsurface ice melt. We use a nonlinear least squares solution to determine the value of the recharge temperature and salinity, as well as the excess air injection and glacial meltwater content throughout the water column and in the precursor to Antarctic Bottom Water. The noble gas-derived recharge temperature and salinity in the Weddell Gyre are $-1.95°C$ and 34.95 psu near 5500 m; these cold, salty recharge values are a result of surface cooling as well as brine rejection during sea ice formation in Antarctic polynyas. In comparison, the global value for deep water recharge temperature is $-0.44°C$ at 5500 m, which is $1.5°C$ warmer than the southern hemisphere deep water recharge temperature, reflecting a distinct contribution from the north Atlantic. The contrast between northern and southern hemisphere recharge properties highlights the impact of sea ice formation on setting the gas properties in southern sourced deep water. Below 1000 m, glacial meltwater averages 3.5‰ by volume and represents greater than 50% of the excess neon and argon found in the water column. These results indicate glacial melt has a nonnegligible impact on the atmospheric gas content of Antarctic Bottom Water.

1. Introduction

Deep water formation in the Southern Ocean is a seasonal process that occurs in the subpolar gyres to the south of the Antarctic Circumpolar Current (ACC). Dense shelf waters form primarily in katabatic wind polynyas [*Bromwich and Kurtz*, 1984], but also as a result of ephemeral latent heat polynyas [*Cheon et al.*, 2015]. These shelf waters entrain midlayer waters derived from the Circumpolar Deep Water (CDW) of the ACC close to the shelf and slope regions of Antarctica to form Antarctic Bottom Water (AABW) [*Talley*, 2008]. Early concepts held that as much as 70% or more of total AABW originated in the Weddell Sea [*Hoppema et al.*, 2001; *Jacobs*, 2004; *Meredith*, 2013]. However, recent studies indicate that a significant flow of dense water enters the Weddell Gyre from the east from formation regions close to the Amery Ice Shelf and Cape Darnley Polynya [*Ohshima et al.*, 2013; *Jullion et al.*, 2014; *Naveira Garabato et al.*, 2014].

Biogeochemically, deep water formation and the strength of photosynthesis in the Southern Ocean are thought to be important to the sink of anthropogenic carbon [*Le Quéré et al.*, 2007], and important as a climate feedback on the glacial-interglacial cycles of the Pleistocene [*Marinov et al.*, 2006; *Hain et al.*, 2010]. Both the sink and the feedback are related to the exchange of carbon between the deep ocean and the atmosphere, which in turn depends on the strength of the biological and solubility pumps. The solubility pump is most directly related to the rate of deep water formation, and consequently the strength of the carbon sink may change if the rate of deep water formation changes [*Nicholson et al.*, 2010; *Meredith et al.*, 2011; *de Lavergne et al.*, 2014]. But the solubility pump for any gas also depends on the gas saturation at the time that deep water is formed. Gas saturation in turn is a function of water temperature [*Hamme and Emerson*, 2004], wind speed [*Wanninkhof*, 1992], air bubbles in the surface ocean [*Liang et al.*, 2013], and sea ice
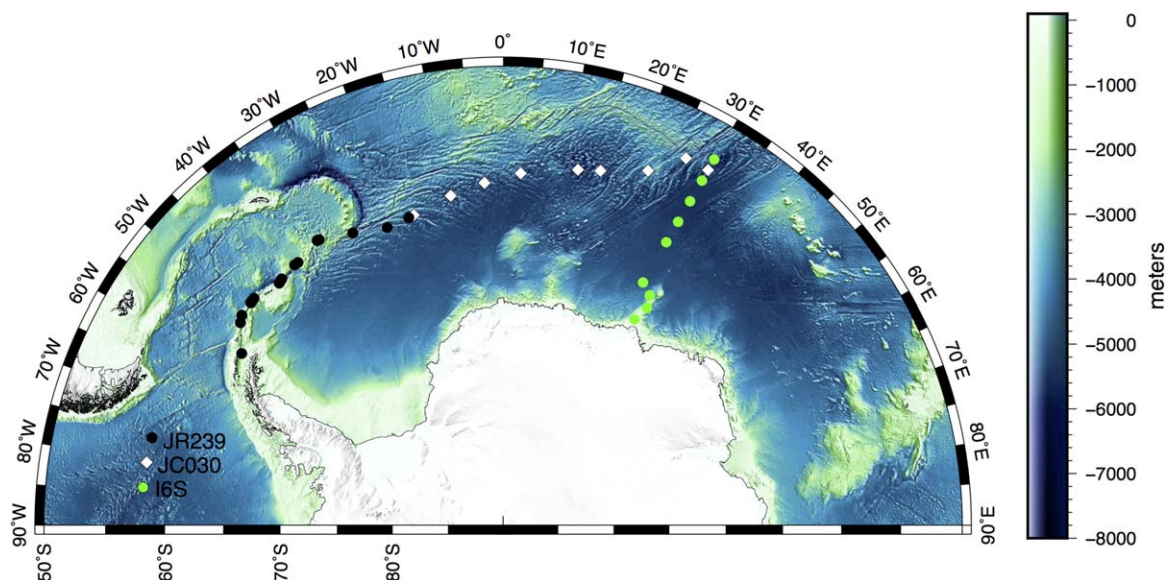
Figure 1. Map of the hydrographic stations in JR239, JC030, and I6S where noble gases and helium isotopes were collected in the Weddell Sea for this analysis.

cover [*Loose et al.*, 2014]. Wind speed and air bubble injection may both have been stronger in the Pleistocene Southern Ocean but sea ice cover may also have been greater making it a challenge to interpret how the solubility pump may have operated during the Last Glacial Maximum (LGM).

In the Southern Ocean, a significant portion of AABW forms from Circumpolar Deep Water (CDW), a water mass that is old with a heavy burden of remineralized carbon [*Gruber et al.*, 2009]. This water upwells in the circumpolar ACC belt, and intrudes into the subpolar gyres in modified form. The relative age of this water mass is reflected in the low $\Delta^{14}C$ values that persist throughout the Southern Ocean, particularly south of the Antarctic Polar Front (APF). The formation processes by which CDW contributes to new waters are such that exposure time at the surface is often too short to ventilate the large burden of DIC, and consequently the excess DIC that did not outgas can represent an important part of the solubility pump [*Ito and Follows*, 2013]. Ocean models indicate that the most effective way to keep atmospheric CO_2 low (i.e., during a glacial epoch) is to stem the Southern Ocean off-gassing of CDW [*Toggweiler*, 1999].

In this study, we explore the imprint of the physical processes that are recorded in the noble gases as surface water becomes deep water during polynya-driven convection. We estimate the effect of air injection by bubbles, the temperature, and salinity of sinking shelf water as it leaves the surface to become deep water, and we account for the input of glacial meltwater to Antarctic Bottom Water. Finally, we use these results to analyze the differences in recharge properties of deep water that is sourced from the southern hemisphere versus water that represents a combination of northern and southern hemisphere recharge.

2. Methods for Determining Recharge Properties

2.1. ANDREX and I6S Cruises

The noble gas and helium isotope data used here were collected in the Atlantic sector of the Southern Ocean along a section that extends east-northeast from the Antarctic Peninsula, beginning at 62°S, 56°W, and terminating near 54°S, 30°E (Figure 1). This section was completed in two legs, as part of the NERC-funded ANDREX (Antarctic Deep water Rates of Export) project. The first leg was completed aboard the RRS *James Cook* in January 2009—corresponding to the stations east of 19°W, and the second leg was completed aboard the RRS *James Clark Ross* approximately one year later in March–April 2010 [*Jacobs*, 2004; *Jullion et al.*, 2014]. Station 68 was occupied during both cruises for intercomparison purposes; noble gases and helium isotopes were measured in both cases giving an opportunity to investigate any potential differences that one year may have had on the tracer fields.

Table 1. The End-Member Properties Used in the Nonlinear OMPA Solution[a]

	RW	GMW	CDW	Air
[Ne] μmol kg^{-1}	m.s.	0.086544	0.0081	18.18 ppmv
[Ar] μmol kg^{-1}	m.s.	44.46	16.30	0.93%
[Kr] μmol kg^{-1}	m.s.	0.00543	0.00395	1.14 ppmv
[Xe] μmol kg^{-1}	m.s.	0.000414	0.000590	87 ppbv
δ^3He, %	-1.7	0	10.1	0
θ, °C	-1.9	-88	1.5	N/A
Sal, psu	m.s.	0	34.64	N/A

[a]The term m.s. signifies this value is calculated as part of the OMPA model solution. Values for air content are not given in μmol kg^{-1}, rather in mixing ratios. The temperature of RW is distinct from θ_R because of faster heat exchange at the air-sea interface, so the temperature of ice shelf water is used as the value of T in RW [*Foldvik et al.*, 2004].

Noble gas samples were also collected and analyzed along the CLIVAR section I6S, during February–March 2008. This section extends north from 68°S along the 30°E meridian from the coast of Antarctica to the coast of Africa. The noble gas samples only include a subset of this section—the part along the Weddell Gyre from 68°S to 55°S (Figure 1).

2.2. Noble Gas Sampling and Analysis

Noble gas samples were collected from a 24 bottle 10 L Niskin rosette using the copper tube cold-weld method. Water from Niskin bottles is allowed to flow through refrigerator grade copper tubing of either 5/8″ or 15 mm ID copper tubing until all air bubbles have been purged. Subsequently, the ends of the tube are sealed using pneumatic pressure to actuate a hydraulic press equipped with rounded teeth. In the process, the side walls of the soft copper tubing are pressed together producing an air-tight seal. Before sampling, the inner volume of the copper tube is decreased by flattening the tube. After cold welding the sample, the flat section of the tube is made round again, effectively increasing the volume inside the tube and producing a vacuum inside the sample. The increase in volume allows for thermal expansion of the water as it warms. By shaking the tube after rerounding, an audible "pop" can be heard, which we believe is caused by cavitation or dissolved gas coming out of solution to fill the void space. This is confirmation of a leak-tight seal. Finally, the copper tube sample is rinsed in ethanol or deionized water to ensure the surface is free from seawater, oils, and other dirt that can lead to corrosion. Leaky copper tubes can also be recognized by corrosion at the tips.

The copper tube sample yields a total of 45 g of seawater on average. In the laboratory, the samples are inserted into a vacuum-tight bellows chamber. The chamber is sealed and a vacuum of at least 10^{-7} torr is drawn on the chamber. Samples are opened at both ends by compressing the chamber along the bellows. Subsequent to opening the samples, dissolved gas is quantitatively extracted from the water and captured inside an aluminosilicate glass bulb that is maintained at -196°C using a liquid nitrogen bath. After gas extraction, the bulbs are attached to a dual mass spectrometric system and analyzed for He, Ne, Ar, Kr, and Xe according to *Stanley et al.* [2009a]. The noble gases are isolated on two cryogenic traps and selectively warmed to sequentially release each gas into the Hiden Quadrupole Mass Spectrometer (QMS) for measurement by peak height manometry [*Lott*, 2001]. The reproducibility from duplicate samples is listed in Table 2. Precision was 0.5% or better for Ar, Kr, and Xe and approximately 1% for He and Ne.

Table 2. The Precision of Noble Gas Samples Estimated From by the Coefficient of Variation Between Duplicate Samples Collected From the Same Niskin Bottle and Analyzed Using the Same Noble Gas Analysis Protocol

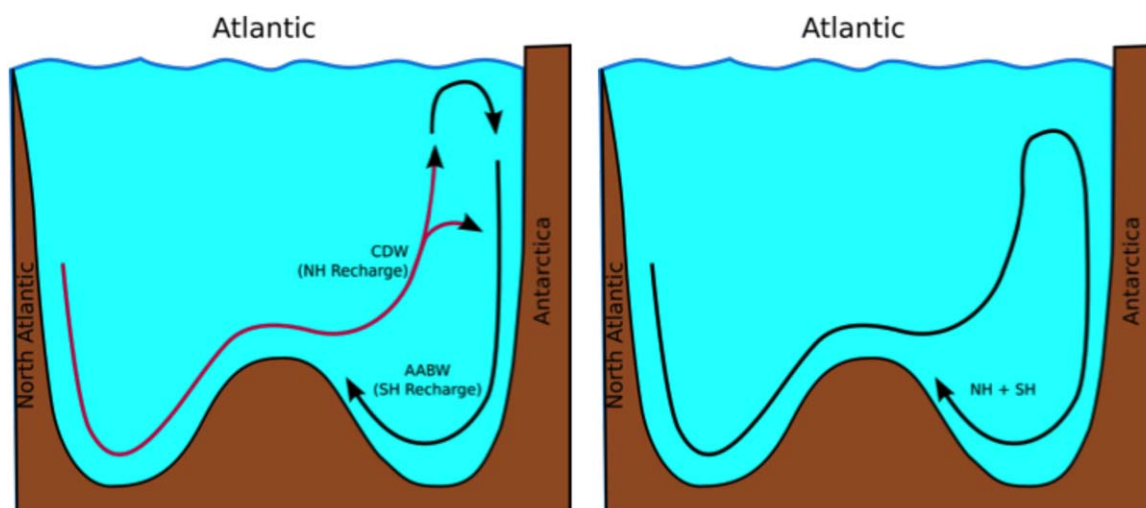|	JR239 Dupes	JC030 Dupes	I6S Dupes	St. 68 Versus 27
	1 σ (%) (N = 7)	1σ (%) (N = 4)	1σ (%) (N = 5)	1σ (%) (N = 8)
δ^3He	0.15	0.04	0.03	0.36
[He]	0.39	0.64	0.89	1.11
[Ne]	0.33	0.23	0.59	0.78
[Ar]	0.12	0.39	0.22	0.33
[Kr]	0.20	0.50	0.31	0.53
[Xe]	0.33	0.50	0.50	0.59

Figure 2. After *Sigman et al.*, [2010] schematic of two OMPA circulation scenarios. (left) The separation between CDW whose precursor is the North Atlantic Deep Water (NADW) upwells in the Weddell Sea and is modified by air-sea exchange and mixing before combining with Recharge Water (RW), which is formed on the Antarctic shelves. The two compose Antarctic Bottom Water (AABW). (right) No distinction between northern and southern hemisphere water is drawn. Consequently, RW represents an aggregate or "global" value of surface recharge of the deep ocean from both northern and southern hemispheres.

2.3. Nonlinear OMPA Method for Deep Water Recharge Properties

Ne, Ar, Kr, and Xe are unique among the noble gases because they are inert and their primary reservoir on earth is the atmosphere. The latter distinguishes them from He and Rn, which are both produced by radioactive decay in the lithosphere. The light isotope, helium-3, is also sourced from the mantle and is found in seawater that emanates from ocean spreading centers [*Jenkins et al.*, 2015]. This unique source of Ne through Xe, and their wide range of absolute and temperature-dependent solubility makes them excellent tracers for the physical processes that impact dissolved gases [*Stanley et al.*, 2006, 2009c; *Hamme and Severinghaus*, 2007].

As a consequence, we expect the noble gas concentration in deep water to closely reflect the boundary or formation physical conditions that existed when that water became dense enough to leave the ocean surface and enter the interior. The conceptual picture that frames the details of the processes captured by the noble gases is found in Figure 2 (left). Deep water masses of the ACC are upwelled along density surfaces in the circumpolar belt, and penetrate the subpolar gyres in modified form. These waters can intrude on the Antarctic shelves in certain locations, where air-sea-ice interactions lead to significant heat loss to the atmosphere, and dramatic changes in salinity. At the surface, these waters may experience wind-driven air-bubble injection, possibly mitigated by sea ice. Partial ice cover can restrict equilibration and air-sea gas exchange in some locations and seasons. Cooling primarily takes place from fall into winter; because heat exchange is faster than gas exchange [*Garbe et al.*, 2004], the water may lose heat faster than it gains gas. At cold temperatures, density depends predominantly on salinity; however, the heat loss is a key component of reducing the ocean temperature to the freezing point and subsequently driving the ice production that raises the ocean salinity sufficiently for dense water to be formed. The result is gas composition with a slight excess in Ne from bubbles, and a deficit in Kr and Xe from the rapid cooling. These three processes—cooling, bubble injection, and sea ice formation are reflected in the noble gas concentration found in deep water [*Hamme and Emerson*, 2002; *Hamme and Severinghaus*, 2007; *Nicholson et al.*, 2010].

Another potentially significant source to the noble gas content in deep water is that derived from glacial melt. Both the Ross [*Loose et al.*, 2009a] and Filchner-Ronne Ice Shelves [*Schlosser et al.*, 1990] produce glacial melt through interaction with high-salinity shelf water ($\gamma^n > 28.63$ which is a precursor to Antarctic Bottom water [*Orsi et al.*, 2002]). Meltwater concentration also reflects a unique dissolved and noble gas signature, and the concentration of meltwater is regularly estimated from dissolved gases as well as temperature and salinity [*Jenkins and Jacobs*, 2008]. However, these estimates are typically carried out using water in close geographic proximity to ice shelves. Here, we explore the potential for a nonnegligible quantity of meltwater in deep water, further from the source.

The method of reconstructing the recharge temperature from noble gas concentration is known as the noble gas paleothermometer (NGPT) and it has been applied to water taken from deep aquifers that infiltrated them
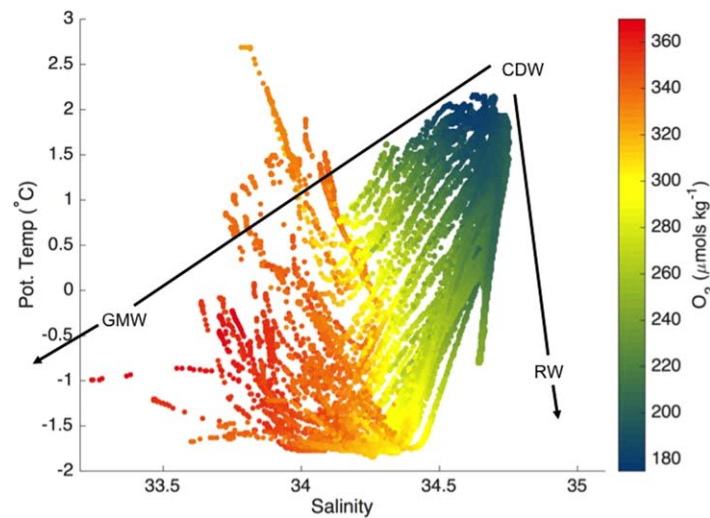
Figure 3. CTD measurements of potential temperature, salinity, and dissolve O_2 during the ANDREX/I6S cruises. The black lines indicate linear hypothetical mixing lines between CDW, glacial meltwater (GMW), and recharge water (RW).

during both modern and glacial periods [*Stute and Schlosser*, 1993, 2000; *Aeschbach-Hertig et al.*, 1999; *Ballentine and Hall*, 1999; *Aeschbach-Hertig and Solomon*, 2013]. Here we borrow the analogy of aquifer recharge to examine the conditions of deep ocean recharge and expand upon the application and interpretation to account for the role of sea ice and glacial meltwater in producing the noble gas concentrations. The noble gas paleothermometer model has been formulated with a variety of approaches [*Aeschbach-Hertig et al.*, 2008], but the version that most closely matches the qualitative picture described above is as follows:

$$C_{i,sw} = C_i^{eq}(S_R, \theta_R, P) + C_i^{exc}; C_i^{exc} = A\chi_i \tag{1}$$

The term, $C_{i,sw}$ is the observed noble gas concentration in surface water (i = Ne, Ar, Kr, or Xe), and it is the sum of the equilibrium gas content, C_i^{eq} and the excess gas content. C_i^{eq} depends empirically on seawater salinity, temperature, and atmospheric pressure. Perturbations in the surface ocean properties of temperature, salinity and atmospheric pressure can all lead to disequilibrium between the observed gas concentration ($C_{i,sw}$) and the equilibrium or "saturated" gas concentration C_i^{eq}. The potential for disequilibrium is represented as follows: Exchanges of heat or freshwater that can lead to changes in temperature and salinity, but may not be accompanied by an equivalent exchange of gas, are accounted for by allowing S and θ to vary as free parameters in the model. Here, we use the terms S_R and θ_R, the "recharge" salinity and "recharge" potential temperature to emphasize that these are end-member values reconstructed from the dissolved gas concentrations. S_R and θ_R are likely to be distinct from the in-situ values of S and θ, because they reflect the disequilibrium that exists between the observed noble gas concentrations and the noble gas concentration that is predicted from in-situ S and θ. Because the empirical solubility functions are incorporated into equation (1), the unique response of each noble gas to changes in temperature and salinity is accounted for. The other significant source of surface ocean gas disequilibrium – sea level pressure - has been fixed at P = 0.97 atm, which is descriptive of the persistent low pressure over the Antarctic coast [*Allan and Ansell*, 2006]. This limits some variability in the final solution, but is a necessary tradeoff in comparison with the other sources of noble gas variability that exist.

The gas concentration is expressed as moles of gas per kg of seawater. Likewise, A is the total quantity of excess air in mol kg^{-1} of seawater that has been forced into solution. In the absence of sea ice formation, the value of θ_R depends on the competition between seasonal heating/cooling and the rate of air-sea gas exchange. Whereas the equilibration time for non-buffered gases is on the order of a month in the ice-free surface ocean [*Ito et al.*, 2004; *Bender et al.*, 2011], this equilibration time is likely extended by the presence of sea ice, therefore θ_R may be more representative of a weighted average of annual surface temperature.

Equation (1) describes the properties of surface water at the time of subduction, when surface ocean processes (including air-sea exchange and sea ice formation) cease to influence the noble gas content of the water parcel. This formulation is equivalent to previous versions of the noble gas paleothermometer.

However, some additional modification to the NGPT is necessary to account for mixing and entrainment from other water masses. In this case, we utilize a relatively broad description of water mass properties for the Weddell Gyre. CDW is low in oxygen due to remineralization of organic carbon (Figure 3) and high in

[3]He by interaction with mid-ocean ridges [*Lupton and Craig*, 1981], and enters the Weddell Gyre from the north [*Garabato et al.*, 2007]. CDW is the warmest water mass (up to $\theta = 2.1°C$ in the ANDREX section, Figure 3) and is commonly found between 200 and 2000 m [*Sievers and Nowlin*, 1984]. This characterization can account for the majority of variability that we observe in the water mass properties; however, it fails to distinguish entirely between upper and lower CDW, which causes broadening in the θ-S distribution above $\theta = 1.5°C$ and $S = 34.5$ (Figure 3). The addition of cold, salty shelf water [*Årthun et al.*, 2012], and glacial meltwater [*Hellmer*, 2004] complete the admixture of water masses that produce Weddell Sea Bottom Water (WSBW) and Weddell Sea Deep Water (WSDW). Collectively, WSBW and WSDW comprise the AABW in the Weddell Sea.

We can separate the components or water types in the hydrographic mixture using the Optimal Multiparameter Analysis (OMPA) [*Poole and Tomczak*, 1999]. Briefly, OMPA requires a nonnegative least squares solution to a system of linear equations that describe the observed tracer content in terms of end-member properties that have been derived based on physicochemical limits or observations of the water mass in its pure form. We follow the approach of *Tomczak* [1981] and define the end-member values based upon the linear portion of the mixing line in temperature-tracer space, where tracer is any of the other gas tracer constraints. The OMPA equation for the three source waters on which we are focused in the Weddell Gyre is written as follows:

$$C_{i,SW} = f_{RW}C_i^{RW} + f_{GMW}C_i^{GMW} + f_{CDW}C_i^{CDW} \tag{2}$$

Here, f_{RW}, f_{GMW}, and f_{CDW} are the fractions of Recharge water, Glacial meltwater, and CDW that compose the admixture. The end-member values for RW, GMW, and CDW are found in Table 1.

This system is solved in an error-minimizing sense, provided there are as many water mass tracers as free parameters. Aside from the water mass tracers, OMPA introduces an additional constraint by requiring that the water mass fractions sum to 1: $1 = f_{RW} + f_{GMW} + f_{CDW}$. In this version of the OMPA, we seek to determine the recharge properties of surface water at the time of convection, and to estimate the total air content that has been introduced by bubble injection. Pure air is not a source water type—it has a negligible enthalpy and the addition of air has no influence on the salt content of the water. Therefore, the air content is not explicitly considered in the statements on heat and salt conservation (equation (4)). This leads to a modified-OMPA equation:

$$C_{i,SW} = f_{RW}\left[C_i^{eq}(S_R, \theta_R) + A\chi_i\right] + f_{GMW}C_i^{GMW} + f_{CDW}C_i^{CDW} \tag{3}$$

Equation (3) depends implicitly on the S_R and θ_R through the empirical gas solubility relations, so we permit the OMPA solution to determine the values of these properties. Therefore, the solution to equation (3) requires a nonlinear optimization to allow for iteration and convergence around the recharge temperature and salinity. As with the NGPT method [*Aeschbach-Hertig et al.*, 1999], we use a bounded nonlinear solver implemented in Matlab[TM].

In total, there are six free parameters—S_R, θ_R, A, f_{RW}, f_{GMW}, and f_{CDW} which requires at least six water mass tracers. In addition to the noble gases, potential temperature (θ), salinity, and the continuity constraint are added to the system described in equation (3),

$$1 = f_{RW} + f_{GMW} + f_{CDW}$$
$$S = f_{RW}S_R + f_{GMW}S_{GMW} + f_{CDW}S_{CDW} \tag{4}$$
$$\theta = f_{RW}\theta_{SW} + f_{GMW}\theta_{GMW} + f_{CDW}\theta_{CDW}$$

The potential temperature of shelf water during convection (θ_{SW}) is fixed at $-1.9°C$ (Table 1), instead of using θ_R from the NGPT, because of differences in the rate of air-sea heat and gas exchange.

Here we also make use of the saturation anomaly, which is defined as the percent deviation from saturation equilibrium with moist air, as determined from the in situ potential temperature and salinity,

$$\Delta_i = \left(\frac{C_i^{in\ situ}}{C_i^{eq}(S, \theta)} - 1\right) \times 100 \tag{5}$$

The anomaly indicates whether the given sample of water would want to consume or release gas if it was lifted to the surface and brought into contact with the atmosphere. The equilibrium solubility values (C_i^{eq}) are
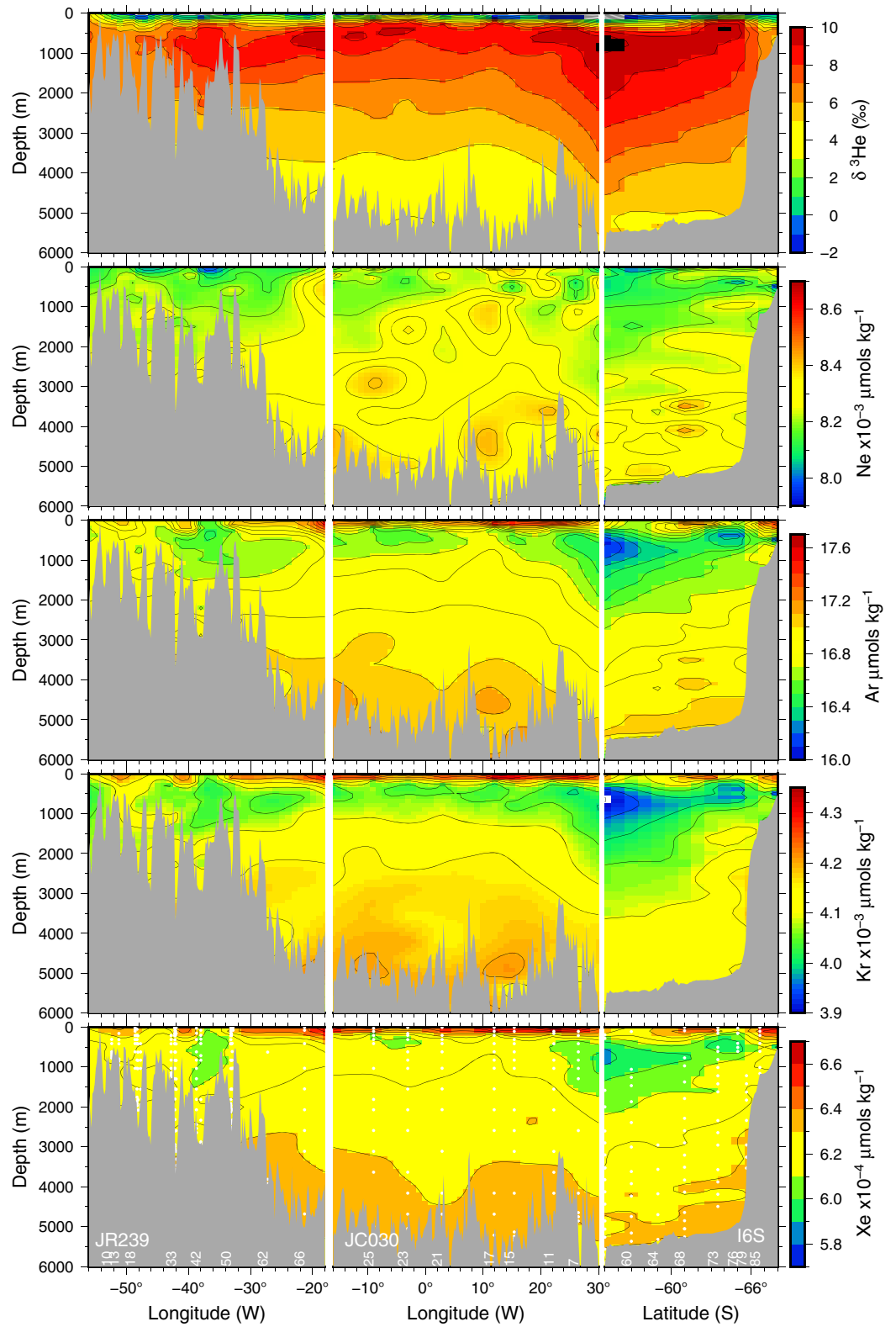
Figure 4. Tracer distributions of δ^3He, Ne, Ar, Kr, and Xe along the two ANDREX cruises (JR239 and JC030) and along the CLIVAR I6S line. The white numbers at the bottom match the station enumeration used during each cruise.
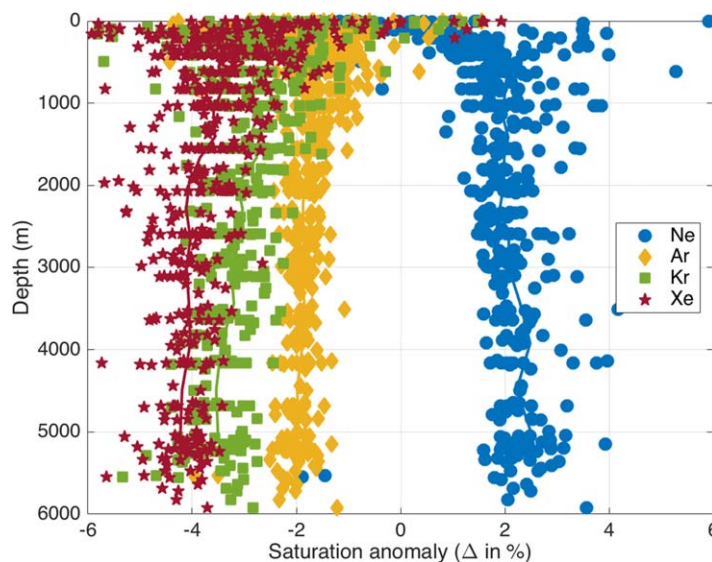
Figure 5. The saturation anomaly of the five noble gases, calculated using the in situ potential temperature and salinity from CTD hydrography.

calculated using the solubility functions of *Weiss*, [1971] for He and Ne, *Hamme and Emerson* [2004] for Ar, *Weiss and Kyser* [1978] for Kr, and *Wood and Caputi* [1966] for Xe, after a 2% decrease in the solubility values as suggested by *Hamme and Severinghaus*, [2007].

3. Results

3.1. Noble Gas Distributions in the Atlantic Sector of the Southern Ocean

Broadly speaking, the distribution of heavier noble gases (Figure 4) largely reflect the distribution of temperature that is found in the Weddell Gyre. Neon is the exception—its concentration increases almost monotonically from its lowest value of $\sim 7.91 \times 10^{-4}$ μmols kg^{-1} at the ocean surface to maximum of 8.6 $\times 10^{-4}$ μmols kg^{-1} below 5000 m. The northernmost deep waters along the zonal section (Figure 4, middle) contain the highest neon concentration. This monotonic tendency does not hold for Ar, Kr, and Xe. These three gases all show the greatest concentration near the ocean surface and then decrease to their lowest values in the core of CDW between 200 and 1500 m. Below 2000 m, their concentrations begin to increase again, and they are maximal in the deep water below 5000 m. This pattern is a reflection of the temperature effect on gas solubility, i.e., that warmer water holds less gas. The distribution of δ^3He follows a reciprocal distribution compared to Xe; its lowest value near the ocean surface is -1.7% and δ^3He is highest in the core of CDW.

A similar dichotomy between Ne and the other noble gases is apparent in the saturation anomaly (Δ, Figure 5). Ar, Kr, and Xe first decrease from the surface to approximately 200 m depth and then gradually increase from $\sim$1000 m to the seafloor. Ne does not decrease from 0 to 200 m, instead the ΔNe increases quickly from 0 to 200 m and then more gradually thereafter, although the scatter in the data at the surface makes the Ne trend appear less pronounced. The trends in saturation anomaly with depth are consistent with profiles from *Hamme and Severinghaus* [2007] from the deep water sampled in the North Pacific below 1000 m. Yet, both *Hamme and Severinghaus* [2007] and *Emerson et al.* [2012] find Ar excesses in the permanent thermocline, which they interpret to arise from low diapycnal mixing in that area. The thermocline at 40°N has very different ventilation history than in the Weddell Gyre. The CFC tracer ages range from 23 to 27 years [*Emerson et al.*, 2012], indicating that the thermocline is ventilated locally in the North Pacific. In comparison, the Southern Ocean thermocline is composed mostly of CDW, the remnant of NADW where cooling and rapid convection can lead to gas deficits, even in argon.

The magnitudes of the values of Δ_i reflect the large differences in solubility between Ne and Xe. In proximity to the air-sea interface, all of the gases are closest to saturation equilibrium. Moving deeper, Ar, Kr, and Xe are all undersaturated by 0.5–2%, with the more soluble gases (Kr and Xe) showing the most depleted saturation anomaly. These gas deficits hint that upon last contact with the atmosphere the water lost heat faster than the gas could equilibrate. The deficit in heavy noble gases can also reflect an addition of glacial meltwater.

On the other hand, both neon and helium are over saturated: Ne by 3% and He by more than 7% below 5000 m. These excesses reflect the addition of glacial meltwater and the injection of air bubbles at the ocean surface. They also reflect the fact that neon and helium solubility do not respond as strongly to the decrease in temperature as Ar through Xe. The changes in Δ_i that are caused by changing temperature, by
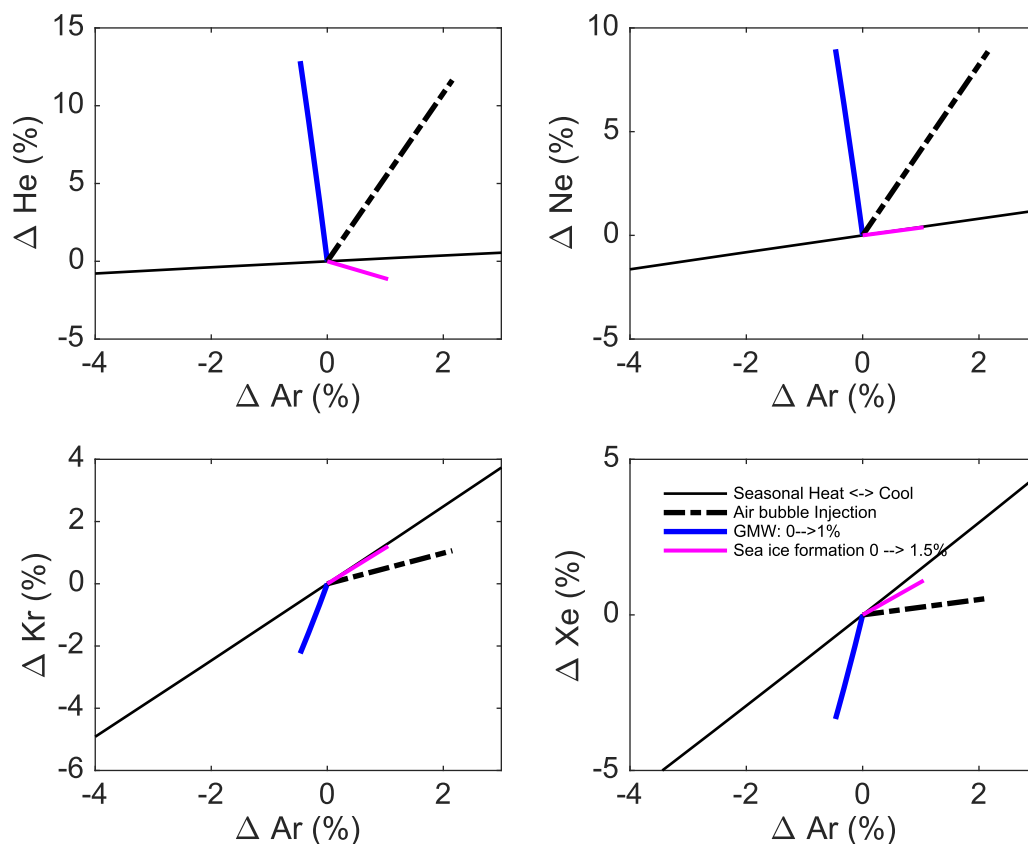
Figure 6. Changes in the noble gas saturation anomaly as a result of seasonal heating and cooling (thin black line), air bubble injection (dashed black line), up to 1% glacial meltwater addition (solid blue line), and 1.5% sea ice formation (solid magenta line), which is equivalent to 4.5 m of sea ice formation above a 300 m water column.

the addition of up to 1% glacial meltwater, by the injection of air bubbles at a constant wind speed of 10 m s^{-1} for 25 days, and by the formation of 1.5% sea ice over the water column are illustrated in Figure 6. This is similar to the scenario presented by *Loose and Jenkins* [2014] who demonstrated that the light and heavy noble gases are able to distinguish air bubble injection by wind and waves from glacial meltwater addition. This distinction between GMW and air bubbles relies primarily on the effect that freshening and latent heat have on gas solubility. That is, when glacial ice melts in seawater, there is a large decrease in temperature, consumed by the latent heat of fusion. This cooling and freshening of the admixture increases the solubility for gases like Kr and Xe. For these two gases the increase in solubility is greater than the addition of gas trapped in glacial ice [*Martinierie et al.*, 1992]. Consequently, the saturation anomalies for Kr and Xe are *decreased* by glacial melt. The trend in Ne is toward a strong increase in Δ_i—reflecting that air trapped in ice has very significant quantities of Ne and these gases have a very low solubility in water. Pure glacial meltwater has a saturation anomaly of $\Delta Ne = 940\%$ [*Hohmann et al.*, 2002], demonstrating their elevated gas concentration, compared to ambient seawater at the freezing point. $\Delta Kr = -20\%$ and $Xe = -41\%$ in pure GMW.

3.2. Nonlinear OMPA Solution to the Noble Gas Paleothermometer

Solving equations (3) and (4) was carried out using δ^3He, Ne, Ar, Kr, and Xe as tracer constraints from gas samples collected during the two ANDREX and the single I6S cruises. In the OMPA solution, all water mass fractions are constrained to vary between 0 and 1 [*Tomczak*, 1981]. Here, we employ additional constraints by adding upper and lower bounds to all parameters in the OMPA solution. The bounds on S_R are [0, 40] and on θ_R are [−25, 25]°C, reflecting values that are far outside what would be expected from the solution. The upper bound on air content was established by estimating the total number of mols of air in the space occupied by 1 kg of seawater. One kg of seawater occupies ca. 0.9728 L; at STP this corresponds to 43,391 μmol, and this is the upper bound. We set the lower bound on air to be 0. Whereas there are some
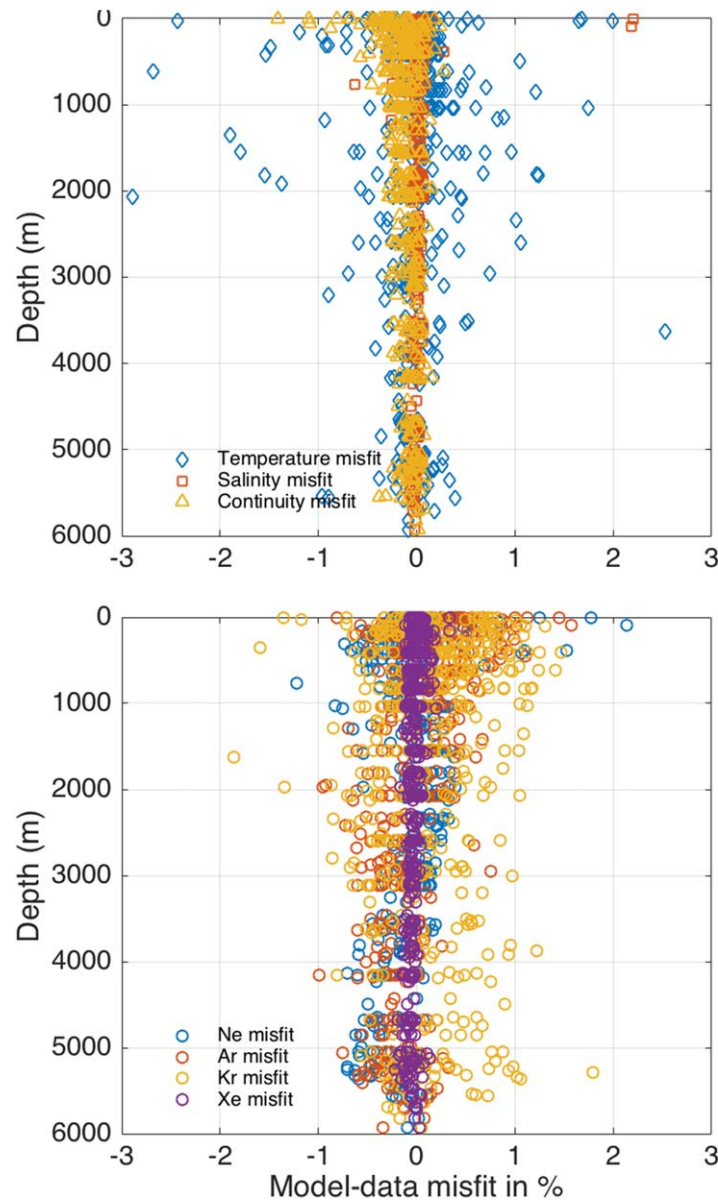
Figure 7. The difference between OMPA reconstruction (model) of the observations, and the ANDREX/I6S observations (data) of temperature, salinity, and continuity values (top plot and equation (4) in the text) and noble gases (bottom plot and equation (3) in the text).

environmental flows, such as aquifers where a decrease in total gas pressure can occur, leading to a negative value for air content [*Aeschbach-Hertig et al.*, 2008], a similar occurrence in the water column would imply cavitation where the water pressure drops below the total gas pressure. Under oceanographic conditions, there is no evidence for this, so we have set the lower bound on air content at 0. To ensure that each equation in (2) and (3) above is given equal weight, we have included a weight matrix in the objective function. We use the reciprocal of the standard deviation to weight the noble gases and we adjust the temperature, salinity and continuity constraint so they have the same weight as the noble gases.

The quality of the OMPA solution is typically evaluated by examining the residuals or model-data misfit. To compute the residuals, we use the output from the OMPA model (f_{RW}, f_{GMW}, f_{CDW}, A, θ_R, and S_R) together with equations (2) and (3) above to reconstruct the in situ values for Ne, Ar, Kr, Xe, θ, and S. The residuals are expressed in % in Figure 7. The average misfit is 0.98% for θ, 0.04% for S, and 0.22, 0.29, 0.41, and 0.05% for Ne, Ar, Kr and Xe, respectively. All noble gas misfits are less than 2%. The continuity misfit is 0.1%. Generally, a misfit of less than 5% is considered to be of sufficient quality to accept [*Karstensen and Tomczak*, 1998]. It is worth noting that the temperature misfit is deceptively large—normalizing by temperature values that are very close to zero inflates the apparent misfit when expressed as "percent." The average absolute value of the temperature misfit is 2.9×10^{-4} °C.

To estimate the uncertainty in the nonlinear OMPA solution, we first tried a Bootstrap resampling statistic using the residuals for each of the noble gases, as well as temperature and salinity [*Mooney*, 1993]. However, we found that random sampling of the residuals caused the solution to converge to the same values of S_R, θ_R, A, f_{sw}, f_{gmw}, and f_{cdw}. This was true for 1000 random resample events at every point in the ANDREX/I6S data set. Setting aside the conclusion that the solution is robust, we next used the noble gas precision (*Pr*) from duplicates in Table 2, and a random sampling from the standard normal distribution—$N(0, 1)$ to perturb the solution,
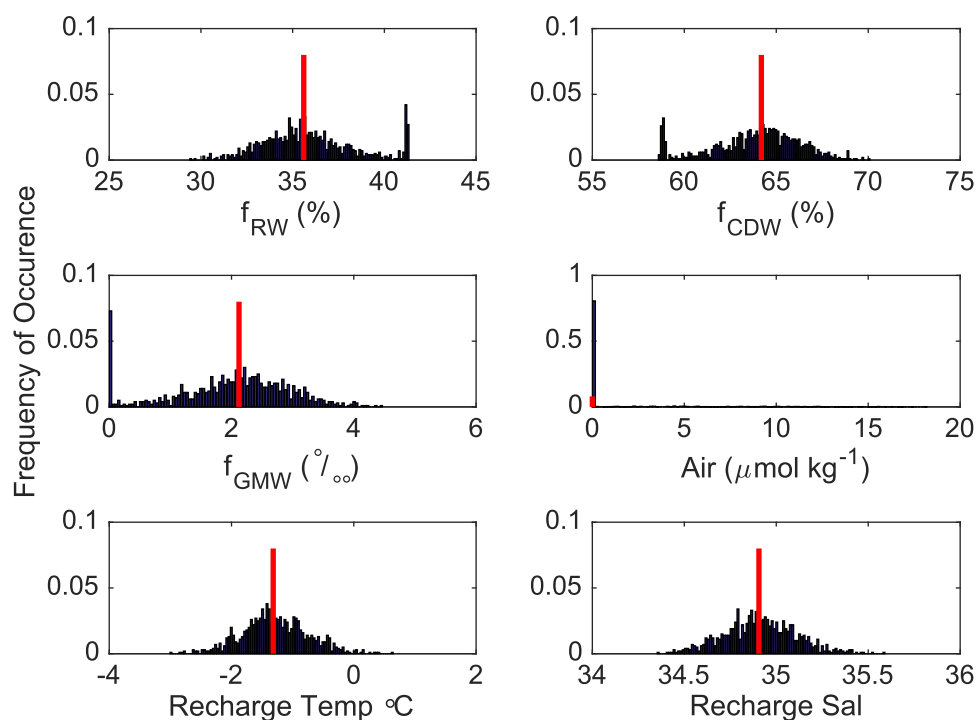
Figure 8. Histogram of the 1000 bootstrap resampling events using a standard normal distribution and the measurement precision to estimate the potential variability in the solution. The red bar represents the mean value—the value that is used as the solution outcome.

$$C_i^{obs}(x,z) = C_i^{obs}(x,z)\left(1 + \frac{Pr}{100} \cdot N(0,1)\right) \qquad (6)$$

This resampling of the population of solutions was used to estimate 95% confidence limits on the solution. The average of the 1000 resampling events is reported as the solution. The value of Pr for θ and S was estimated as 0.001°C and 0.005; the former comes from quoted precision since temperature far exceeds the accuracy of other parameters and the latter is the calculated offset between ANDREX data and GLODAP data as determined by *Jullion et al.*, [2014]. Figure 8 displays a histogram of the bootstrap solutions to the nonlinear OMPA. The parameter space is unimodal for all parameters save Air, which appears to be bimodal near 0 and then follow a uniform distribution between 0 and 15 μmols kg^{-1}. The remainder of the parameters show somewhat asymmetric distributions. Figure 9 displays the depth profile of each parameter separated by the three cruises, JR239, JC030, and I6S. The shaded area represents the $p = 0.95$ confidence interval for each parameter. Both the parameters and their confidence interval have been regionally averaged in Figure 9.

4. Discussion

The vertical distribution of CDW is consistent with a canonical distribution of CDW in the Weddell Gyre: it exhibits the greatest abundance between 500 and 1000 m in the I6S line. This particular section intersected part of the ACC [*Jullion et al.*, 2014] where the core of CDW is found. CDW is at its lowest abundance in the JR239 section, close to the Antarctic Peninsula. Below 2000 m, CDW gradually decreases and RW increases until the two water types are each approximately 50% by volume. Together these two water masses represent 99.5% or more of the total water mass content. The remainder is glacial meltwater and this ranges between 2 and 3‰, below 2000 m. The solution reveals very little excess air content between 1000 and 4000 m. Air content from 0 to 1000 m decreases from 12 to 0 μmol kg^{-1}, with the greatest abundance found in the JC030 line, which is the furthest north. This is at most around 1% of the total capacity of air that can be dissolved in seawater, assuming $\theta = 0$, S = 34. In other words, the excess air content is not a large percentage of the total dissolved gas.
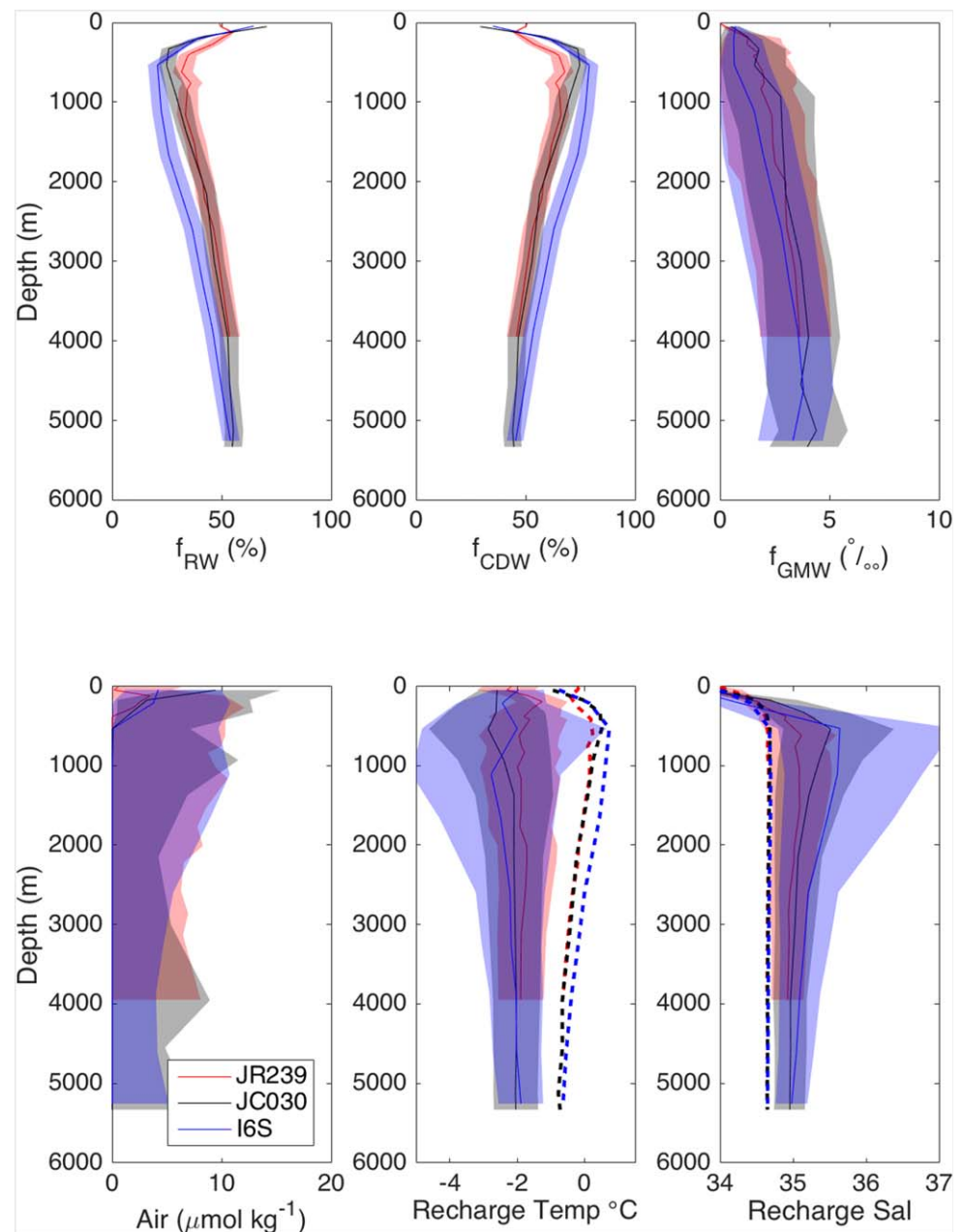
Figure 9. A block average of the nonlinear OMPA solutions for the OMPA parameters, f_{scw}, f_{CDW}, f_{gmw}, air, recharge temperature, and recharge salinity. The transparent-shaded regions represent the block averaged 95% confidence interval on the solution from each of the three cruises. The dashed lines in the temperature and salinity panels are block averages of the measured θ and S from each cruise.

The horizontal average in θ_R ranges from -4 to $-1°$C above 1500 m, but reaches a near constant value of $\sim -1.95°$C for all three cruises, below 2000 m. Recharge salinity is saltier than ambient salinity, ranging from 35.5 psu near 500 m to 34.8 psu at 5500 m. The uncertainty in the solution becomes very large for θ and S above 1500 m and particularly in the area where CDW is maximal. In fact, we excluded 37 samples from above 1500 m because they converged against the temperature and salinity bounds, and we therefore treated these samples as nonconforming with the current mixing model. The degradation in the fit quality is also evident in the θ and S residuals (Figure 7). This can be explained by appreciating that water between 200 and 2000 m has very different origins from much of the rest of the water found in the Weddell Gyre water column. Having originally formed in the North Atlantic, with input from the subtropical Pacific [*Well*

et al., 2003], the core of water found between 200 and 2000 m may not conform well to this water mass model, which dilutes pure CDW with shelf water from coastal Antarctica.

On average, the recharge temperature and salinity are colder and saltier than the majority of the ambient water found in the water column and these recharge values are a reflection of the conditions under which this water has formed. Before we discuss this in more detail, it bears commenting on our choice to allow θ_R and S_R to vary for each noble gas water sample, rather than enforce a single value for all recharge water at all depths. Previous work has indicated that the variation in the values of θ_R and S_R represent the complexity of the downslope ventilation process around Antarctica. *Orsi et al.*, [2002] used CFCs to demonstrate that ventilated water enters a broad range of density horizons, and concluded this was caused by shelf water of varying properties achieving neutral density at a variety of depths. Based upon the observation that binning samples by depth tends to aggregate a significant amount of spatial structure in the three profiles in Figure 9, we elected to solve nonlinear OMPA on a sample-by-sample basis and allow the variation in recharge temperature and salinity to emerge and then evaluate this variation critically against physical oceanographic realism.

4.1. The Effect of Sea Ice on θ_R and S_R

The average value of θ_R below 1000 m is $-1.95°$C. The uncertainty bounds indicate that θ_R could range from -3 to $-1.5°$C. θ_R is 1.3°C colder than the ambient temperature below 1000 m, and is only slightly warmer than shelf water, which ranges from -1.9 to $-2.2°$C [*Årthun et al.*, 2012]. However, shelf water is cooled by its interaction with the Filchner-Ronne Ice Shelf [*Foldvik et al.*, 2004], so it is initially surprising that θ_R should reach this temperature (the cold end-member of glacial melt is accounted for by the GMW water type, see equation (3) and Table 1). Instead, this cold value for θ_R indicates that sea ice may also be a factor in setting the value of θ_R. We will discuss this further in the following paragraphs.

As reported above in section 4.0, the recharge salinity is as much as 0.6 psu saltier than ambient salinity below 2000 m, and S_R exceeds measured shelf water salinities by as much as 0.2 psu [*Foldvik et al.*, 2004]. This increase in salinity is indicative that sea ice may influence the noble gas recharge concentrations. That is, the excess salinity may be an indirect reflection of salt (or more appropriately, solute) rejection during sea ice formation. It has been established through laboratory experiments that most gases are excluded from the ice matrix during freezing [*Killawee et al.*, 1998]. The process of sea ice desalination is complicated and appears to take place in stages; there is some solute exclusion during ice growth [*Loose et al.*, 2009b], and also residual gravity drainage throughout the sea ice life cycle [*Notz and Worster*, 2009]. For this discussion, however, we do not attempt to distinguish between the two but only observe how solute rejection may impact the gas properties of recharge water. During the sea ice growth stage, the exclusion efficiency is not the same for all gases. Instead, there may be a fractionation based upon the Van der Waals Radius of the molecule [*Namiot and Bukhgalter*, 1965]. The process is approximated by the effective partitioning coefficient between the ice and water (k_{iw}),

$$k_{iw} = \frac{C_{ice}}{C_{BW}} \tag{7}$$

C_{ice} is the bulk solute concentration in ice and C_{BW} is the concentration of gas in the "bulk water" beneath the ice [*Killawee et al.*, 1998]. A value of $k_{iw} > 1$ indicates that the gas is preferentially incorporated into the ice. This is not the case for most gases, but there is evidence that for helium $k_{iw} = 1.2–2.1$, and four studies have found values of k_{iw} for neon ranging from $k_{iw} = 0.82$ to $k_{iw} = 0.9$ [*Namiot and Bukhgalter*, 1965; *Top et al.*, 1988; *Malone et al.*, 2010; *Lovely et al.*, 2015]. For Ar, Kr, and Xe, there is some ambiguity in the values of k_{iw}; *Top et al.* [1988] find 0.49, 0.4, and 0.5 whereas *Malone et al.*, [2010] report values of 0.01, 0.06, and 0.05 although these values are referenced to solubility equilibrium, so they are not identical to k_{iw}. For salinity, k_{iw} is also likely to be $\sim$0.3, based upon measurements of bulk salinity in sea ice that usually range between 6 and 10 g/kg of ice [*Eicken*, 2003].

To map the effect of sea ice formation on noble gas saturation anomalies, we use these values for $k_{iw} = 1.9$, 0.9, 0.49, 0.4, 0.5 for He through Xe, and $k_{iw} = 0.3$ for salinity. The effect of ice formation on temperature is not entirely clear. There should be a latent heat release during ice formation, but it is just as likely that this heat is radiated or conducted to the atmosphere. Utilizing these partitioning coefficients, we can plot the tendency Δ_i for each of the noble gases (see Figure 6). This plot is similar to Figure 2 from *Hamme and Emerson* [2002],
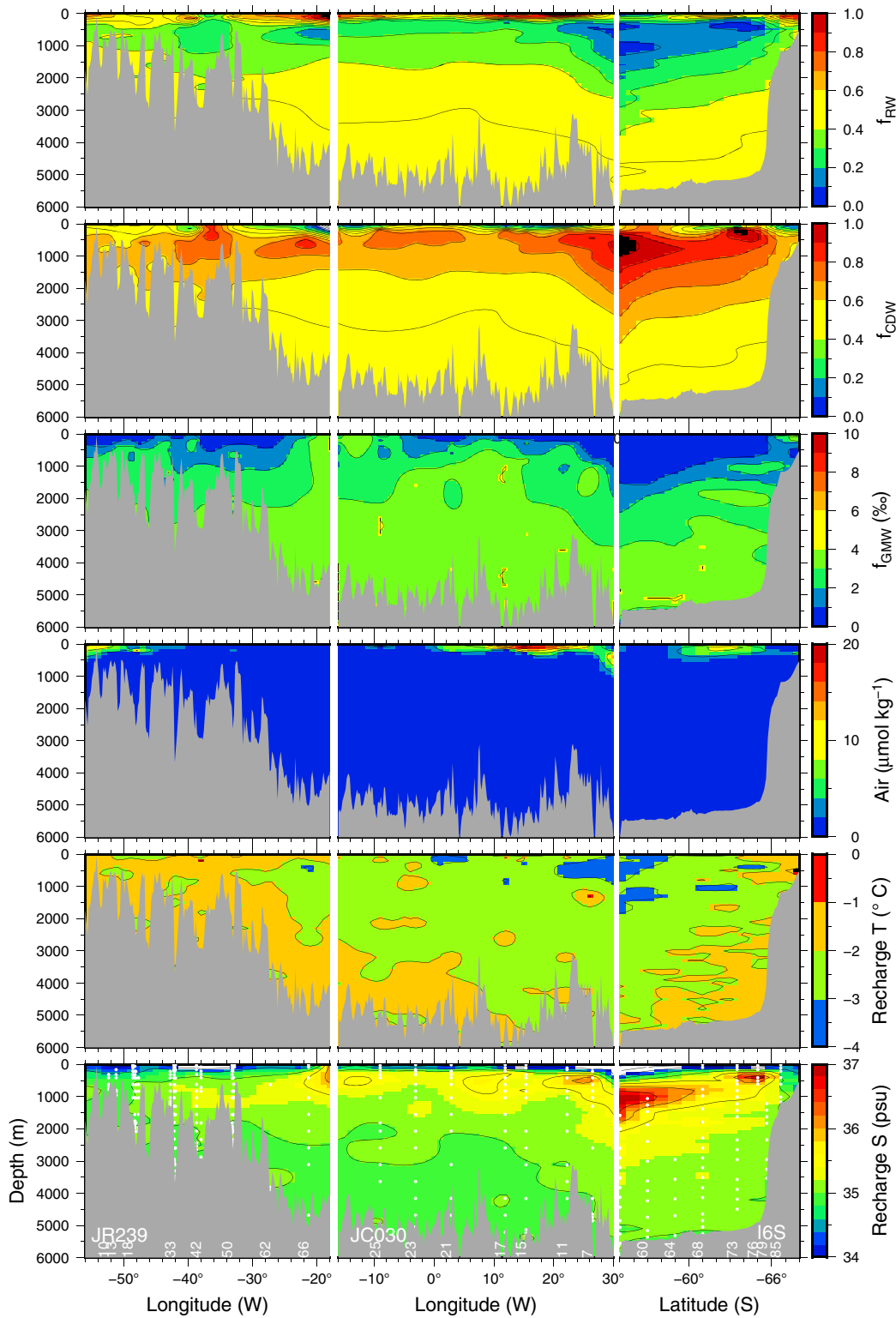
Figure 10. Sections of nonlinear OMPA parameters along the two ANDREX cruises (JR239 and JC030) and along the CLIVAR I6S line. White station numbers at the bottom are the station numbers used during each cruise.

however those authors used a value of $k_{iw} = 1.4$ for Ne. The perturbation, Δ_i, that would result from producing sea ice out of 1.5% of the water column is also plotted in Figure 6. This is equivalent to 4.5 m of ice formation over a 300 m mixed layer, which is similar to the sea ice production estimate of *Årthun et al.*, [2012].

The effect of sea ice production on Δ_i is not predicted to be nearly as strong as air bubble injection nor as glacial meltwater (Figure 6), but the perturbation in ΔHe is greater than 3% and ΔXe is nearly 1.5%, which are fivefold larger than the analytical precision and therefore presumed quantifiable. Sea ice formation (with solute rejection) is parametrically very similar to an increase in water temperature represented by the heating-cooling line in Figure 6. This observation implies the OMPA solution may compensate "sea ice formation" with a colder value of θ_R and indeed it is possible to increase θ_R by assigning a constant value to S_R that is less than 34.8, but this degrades the model-data misfit in all samples below 2000 m, reminding us that the OMPA finds the optimum solution given the tracer constraints. The sensitivity of the solution to these compensating factors is mapped by the uncertainty in Figure 9, and we can see that in all instances below 2000 m, θ_R is less than the ambient temperature, and S_R is saltier than the ambient salinity. Heuristically, the solution of high recharge salinity matches what we understand to take place during deep water formation: that sea ice formation leads to salt injection to the ocean.

Finally, one more line of evidence supports the estimate of recharge salinity greater than 35 psu. *Brown et al.* [2014] used oxygen isotopes to estimate that up to 2.1% sea ice brine fraction (or negative sea ice melt f$_{-SIM}$) can be observed in WSBW. Here we use an "average" value for deep water from their paper (f$_{-SIM}$ = 1.5%) and a representative salinity of sea ice brine (S$_{br}$ = 90) to reconstruct the recharge temperature. Brine salinity can range from 37 to 235‰ depending on the salinity of the formation water, the air temperature, and ice growth rate [*Cox and Weeks*, 1983]. Starting with a surface salinity of 34 psu, we estimate the following recharge salinity,

$$S_R = S_{surface} + 0.015 S_{br}$$
$$= 34 + 0.015(90) \tag{8}$$
$$= 35.35$$

Equation (8) indicates it is plausible to begin with a surface water salinity and add brine from sea ice formation to achieve recharge salinity similar to that estimated by the OMPA solution.

4.2. Glacial Meltwater in the OMPA Solution

The OMPA solution finds undetectable quantities of glacial meltwater across most of the surface ocean (Figure 10). This may in part reflect that the noble gases near the ocean surface can lose the meltwater signal to air-sea exchange. GMW is also lower between 200 and 2000 m, although the solution has the greatest uncertainty in the core of CDW so very little confidence can be associated with any interpretation. Below 1000 m, the meltwater fraction increases to an average near 3.5‰, with the strongest signal found in the water below 1000 m along the JC030 line and below 3000 m on the I6S line.

The solution, therefore, indicates that meltwater is entrained into deep water, although some or all this meltwater signal may not originate in the Weddell Sea, and instead may be transported from deep water formation sites further east along the coast [*Jullion et al.*, 2014]. In the Weddell Sea, some dense shelf water sinks along the retrograde slope beneath the Filchner-Ronne Ice Shelf and produces basal melt near the grounding line [*Bayer et al.*, 1990]. This water exits the cavity as Ice Shelf Water and becomes incorporated into WSBW, which is the densest component of AABW in the Weddell Sea [*Foldvik et al.*, 2004]. However, basal melt occurs at multiple depths in the ice shelf cavity causing glacial melt to become entrained in water masses that are less dense and therefore higher in the water column. It is important to note that some modification of the glacial meltwater likely takes place as a result of marine ice formation [*Bombosch and Jenkins*, 1995]. This ice is bubble-free and slightly saltier than glacial ice [*Oerter et al.*, 1992]. As with sea ice, the incorporation of salt may reflect that some gases are also incorporated into the marine ice [*Killawee et al.*, 1998], but to our knowledge, this marine ice has not been analyzed for noble gas concentration.

For the purposes of comparison, the OMPA estimate of glacial meltwater is within the range of meltwater content that has been observed around Antarctica. Offshore of the Amundsen Sea where warmer CDW comes into direct contact with glaciers, GMW content can reach 20‰ [*Hohmann et al.*, 2002]. In the Ross Sea, GMW content has been observed up to 7‰ near the front of the Ross Ice Shelf [*Loose et al.*, 2009a]. In the Weddell Sea, *Schlosser et al.* [1990] observed Ice Shelf Water spilling off the continental shelf near 73°S and determined from ^{4}He and O-18 that the glacial melt in ISW was 4‰. This is ~0.5‰ more GMW than we estimate further north in WSBW. However, it remains unclear how much ISW is diluted to produce WSBW.

Foldvik et al. [2004] multiplied the ISW flux by 2.7 to get WSBW production. If that can be considered a dilution factor, then the GMW content in WSBW is closer to 1.5‰. The OMPA solution depicts GMW below 4000 m of ~3.5‰, indicating that the OMPA solution might be an overestimate. However, meltwater is found throughout the water column, including in WDW [*Schlosser et al.*, 1990], indicating that glacial melt is found in both precursors (ISW and WDW) to WSBW. Therefore, it is plausible that the meltwater content in WSBW is 3–4‰.

Assuming these results are representative of WSBW and AABW, which is also fed by shelf water around Antarctica, it is interesting to note that the noble gas content in deep water is significantly elevated by glacial meltwater. A 3‰ addition of glacial meltwater increases the Ne concentration in bottom water by nearly 3%, and the ΔNe by a similar amount (Figure 6). In comparison, the same meltwater addition increases Xe concentration by only 0.3%, and decreases ΔXe by around 1%. This implies that the bulk of the Ne saturation anomaly and ~50% of the Xe saturation anomaly in Figure 5 could be attributed to glacial meltwater. For Ar, Kr and Xe, temperature is another major contributing factor to the anomaly. These results imply that GMW has a nonnegligible impact on noble gases found in AABW.

4.3. How Do the Global Recharge Properties Differ From Those of the Southern Hemisphere?

Circumpolar deep water contains a record of deep ocean recharge that takes place in the northern hemisphere. Consequently, we can interpret the water samples from the Weddell Gyre in the framework of the "global" recharge properties by removing the distinction between northern (CDW) and southern (RW) hemispheric origins. Hereafter, we refer to the solution described by equations (3) and (4) as the southern hemisphere (SH) solution. In the present version, represented by equation (9) below, we combine the recharge properties from both hemispheres into a single water type—RW. θ_R and S_R now represent global values of deep water recharge. Figure 2 gives a conceptual picture of how the two NGPT-OMPA scenarios differ in their conception of the circulation. The choice of tracer conservation equations is also slightly altered. Whereas δ^3He is an excellent tracer for separating CDW, it is of little value for the global recharge solution, because it is added to NADW in the deep sea, so it does not measurably contribute to understanding surface processes. For temperature, we can attempt to assign a value to RW that represents some "average" of northern and southern hemisphere water during deep convection. Instead, we opt to use the recharge temperature, despite the acknowledged shortcoming that heat and gas exchange are not always proportional. This allows us to compare the solution to equation (9) for each water sample, independent of a specified end-member value for temperature during convection in RW. In total, we use six tracer constraints left—Ne, Ar, Kr, Xe, and S, θ to solve for five free parameters: f_{RW}, f_{GMW}, A, θ_R, and S_R.

$$C_{i,SW} = f_{RW}\left[C_i^{eq}(S_R, \theta_R) + A\chi_i\right] + f_{GMW}C_i^{GMW}$$
$$1 = f_{RW} + f_{GMW}$$
$$S = f_{RW}S_R + f_{GMW}S_{GMW} \qquad (9)$$
$$\theta = f_{RW}\theta_R + f_{GMW}\theta_{GMW}$$

We refer to equation (9) as the northern + southern hemisphere solution (NH+SH). As with the NH solution, we compute the NH+SH solution for the entire vertical distribution of ANDREX/I6S samples using the same bootstrap sampling with replacement from the error distribution in equation (6).

Not surprisingly, S_R hews more closely to the in situ salinity since f_{GMW} is the only water mass that can cause S_R to deviate from ambient S; however; S_R below 4000 m is greater than S by ~0.1, and this is qualitatively consistent with southern hemisphere sea ice in the deep water admixture. θ_R in the NH+SH solution is nearly 0.3°C warmer than the in situ temperature below 4000 m, and it is 1.5°C warmer than the SH recharge temperature (compare Figure 9 to –11). The increase in recharge temperature reflects a warmer northern hemisphere end-member. The fact that the temperature is warmer than the in situ temperature indicates that the surface temperature at which seawater equilibrates is warmer on average than when that water leaves the surface. Heat diffusion and geothermal inputs would act to make this difference smaller, hence the observed difference in temperature is likely a lower bound.

Whereas there is almost no excess air in RW from the SH solution (Figure 9), the Recharge Water from the NH+SH solution indicates between 10 and 15 μmols kg^{-1} is present throughout the water column, and maximal at the depths of CDW or northern hemisphere recharge. The GMW content in the water column
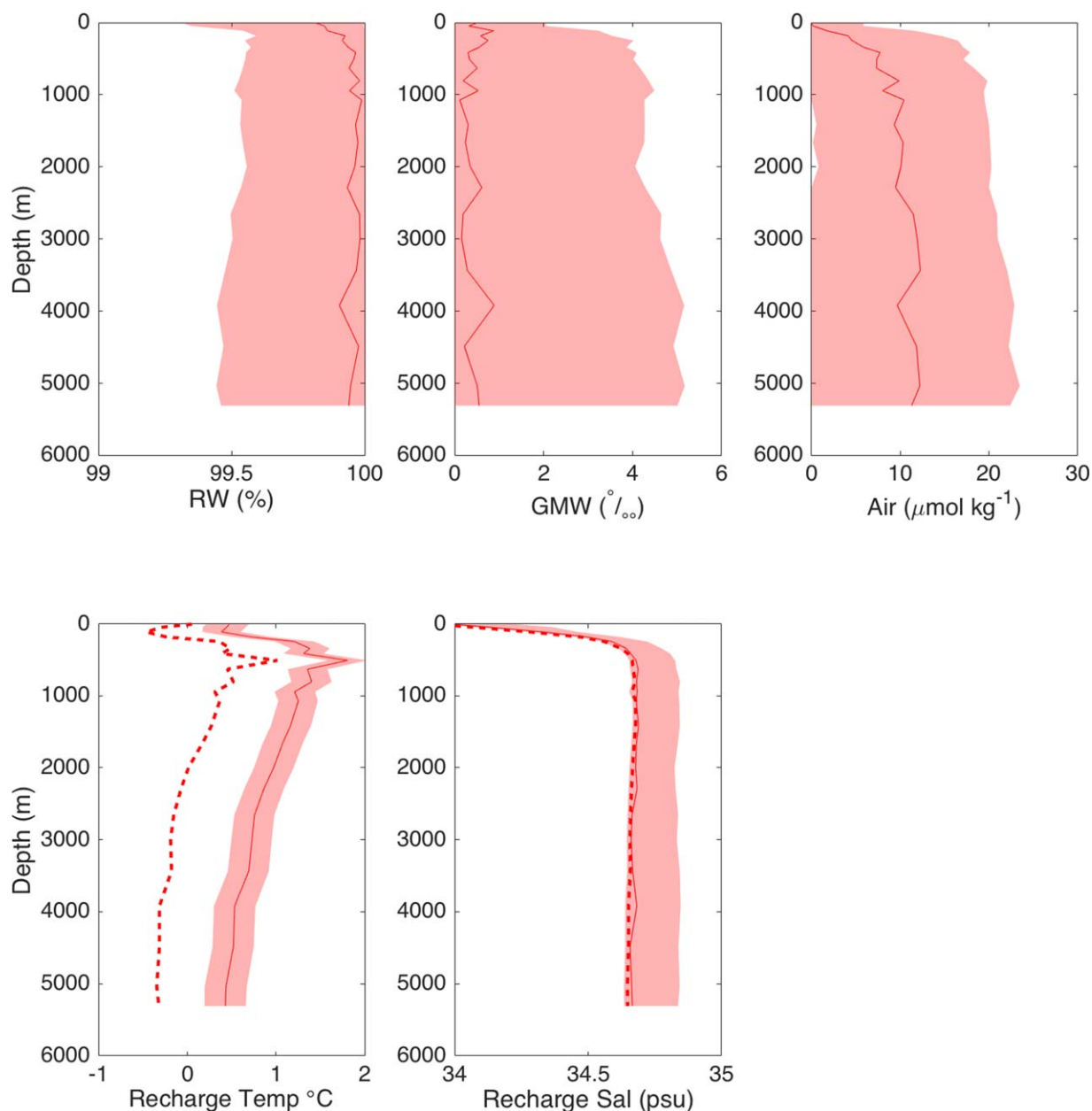
Figure 11. The solution to nonlinear OMPA parameters removing CDW as a water type, so that RW represents an aggregate or "global" value recharge from both the northern and southern hemispheres.

below 2000 m is similar in both SH and NH+SH solutions, indicating 3–3.5‰. Above 2000 m, the GMW content is 2‰ in the NH+SH solution, which differs from the SH solution. The estimate of GMW content should be the same in both solutions, so this shift may reflect the fact that air content and GMW are parametrically similar using the noble gases [*Hamme and Emerson*, 2002; *Loose and Jenkins*, 2014]. If we compare the noble gas content in 12 μmol kg^{-1} of Air, it is equivalent to 2.45‰ glacial meltwater. The uncertainty on both parameters reflects the difficulty of separating the two.

4.4. How Might the NGPT Recharge Properties be Different During the LGM?

Sigman et al., [2010] present a scenario for ocean circulation during the Last Glacial Maximum. In this scenario, water in the deep ocean is colder and more dense than today [*Adkins and Schrag*, 2001]. Consequently, water formed in the North Atlantic may not have penetrated the deep sea. In its place, AABW
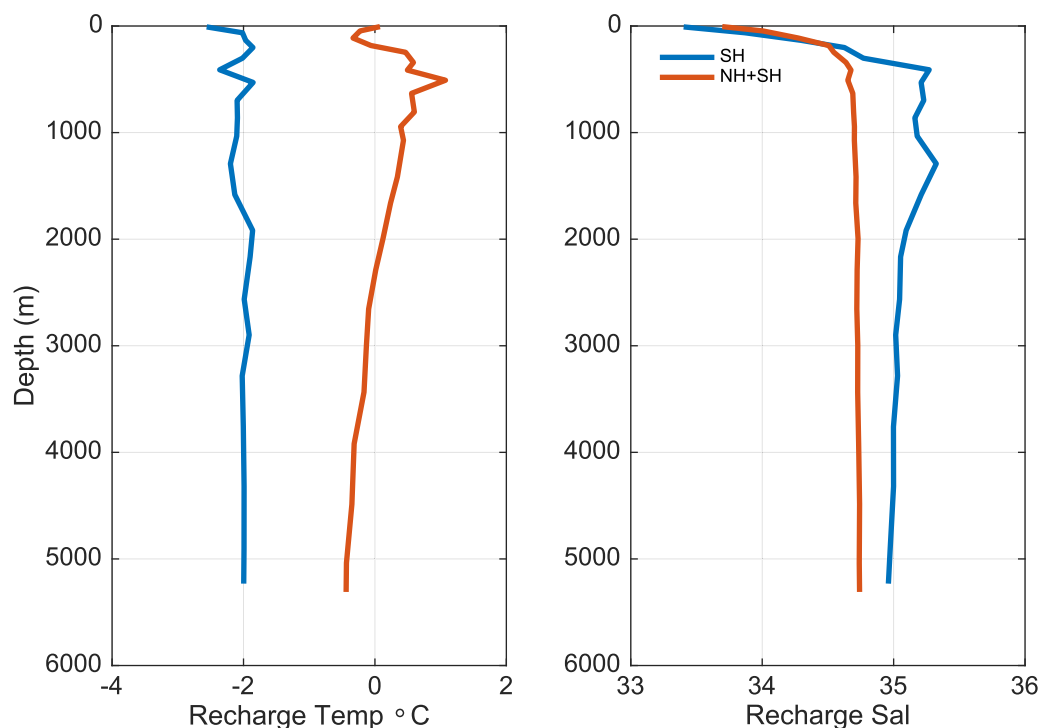
Figure 12. A comparison of the θ_R and S_R values for global (NH+SH) and southern hemisphere (SH) recharge solution. Both results are derived from the OMPA-NGPT solution to water samples from the Weddell Gyre. The NH + SH solution described in section 4.3 represents the combined influence of both CDW and Shelf Water on the global recharge temperature. In comparison, the SH described in section 3 separates the influence of CDW to determine the recharge temperature of southern hemisphere water only.

expanded to fill the entire deep sea, and ventilation (based on radiocarbon ages) may have been slower than it is today [*Adkins and Pasquero*, 2004; *Burke et al.*, 2015].

How might the values of θ_R and S_R during the LGM compare to θ_R and S_R in the modern ocean? If the precursor to CDW (NADW) was not part of the admixture in AABW, the southern hemisphere recharge properties would be more pronounced, leading to colder, saltier recharge water. In this regard, the global values of θ_R and S_R would migrate from the NH+SH solution (blue line) toward the SH solution presented in the first part of the paper—and likely they would be colder and saltier than the modern recharge θ and S (Figure 12).

It is unclear whether glacial meltwater content would be higher in the LGM; on the one hand, an expanded Antarctic Ice Sheet [*Anderson et al.*, 2002] presents more surface area for ocean melting, but ice sheet melt rate depends in part on delivery of heat in the form of water that is above the freezing point [*Holland et al.*, 2008]. While saltier bottom water during the LGM [*Adkins and Schrag*, 2001] lowers the freezing point, it was also probably accompanied by colder water temperatures around Antarctica. Indeed, *Adkins* [2013] argue that it is not possible to produce saltier bottom water without first cooling the water column, meaning the relative temperature difference between ambient water and the freezing point may not have been much larger during the LGM. Whether there is more meltwater in bottom water or not, it may be difficult to distinguish that from excess air, without the aid of temperature as a water mass tracer constraint. The hypothesized presence of sea ice is thought to reduce air-sea gas exchange [*Stephens and Keeling*, 2000], especially the kind of wave-driven exchange that injects excess air. Therefore, we might expect that the water column during the LGM had even less air content than it does today.

5. Conclusions

The OMPA solution to the noble gas paleothermometer gives insight into the formation conditions for water that recharges the deep ocean in the Weddell Sea. The solution finds a recharge temperature of $\sim -1.95°C$, which is similar in temperature to Ice Shelf Water in the Weddell Sea [*Foldvik et al.*, 2004]. The

recharge salinity is saltier than in situ salinity with a value of 35.0 at 5500 m. Based upon our limited understanding of solute exclusion from sea ice, these cold, salty recharge properties reflect not just surface cooling, but the influence of sea ice formation on the noble gas concentrations in deep water. A more thorough empirical understanding of the influence of sea ice on deep water gas budgets would be helpful for interpreting deep-water noble gas concentration, particularly with regard to how the noble gases are partitioned between water and ice.

Porewater from the deep sea might be interpreted using the paleothermometer; the nonlinear OMPA solution indicates that the global recharge temperature is $-0.44°C$ at 5500 m, which is 1.5°C warmer than the southern hemisphere recharge temperature. We predict the global recharge properties would move toward the southern hemisphere recharge properties in the LGM, if water from the North Atlantic ceases to act as a precursor to AABW, as proposed by *Sigman et al.*, [2010] and others.

Finally, the nonlinear OMPA solution finds that glacial meltwater in Weddell Sea Bottom Water is near 3.5‰. Taken together with the small amount of excess air present, this indicates that excess neon (and helium) in AABW may be dominated by meltwater input. This indicates that interpretations of the global distribution of the noble gases need to account for the contribution of meltwater in the Southern Hemisphere. This conclusion is tempered slightly by the observation that it is difficult to separate excess air from glacial melt without the aid of temperature as a water mass tracer.

References

Adkins, J. F. (2013), The role of deep ocean circulation in setting glacial climates, *Paleoceanography*, *28*, 539–561, doi:10.1002/palo.20046.

Adkins, J. F., and C. Pasquero (2004), Deep ocean overturning: Then and now, *Science*, *306*(5699), 1143–1144, doi:10.1126/science.1105531.

Adkins, J. F., and D. P. Schrag (2001), Pore fluid constraints on deep ocean temperature and salinity during the Last Glacial Maximum, *Geophys. Res. Lett.*, *28*(5), 771–774, doi:10.1029/2000GL011597.

Aeschbach-Hertig, W., and D. K. Solomon (2013), Noble gas thermometry in groundwater hydrology, in *The Noble Gases as Geochemical Tracers*, edited by P. Burnard, pp. 81–122, Springer, Berlin.

Aeschbach-Hertig, W., F. Peeters, U. Beyerle, and R. Kipfer (1999), Interpretation of dissolved atmospheric noble gases in natural waters, *Water Resour. Res.*, *35*(9), 2779–2792, doi:10.1029/1999WR900130.

Aeschbach-Hertig, W., H. El-Gamal, M. Wieser, and L. Palcsu (2008), Modeling excess air and degassing in groundwater by equilibrium partitioning with a gas phase, *Water Resour. Res.*, *44*, W08449, doi:10.1029/2007WR006454.

Allan, R., and T. Ansell (2006), A new globally complete monthly historical gridded mean sea level pressure dataset (HadSLP2): 1850–2004, *J. Clim.*, *19*(22), 5816–5842, doi:10.1175/JCLI3937.1.

Anderson, J. B., S. S. Shipp, A. L. Lowe, J. S. Wellner, and A. B. Mosola (2002), The Antarctic Ice Sheet during the Last Glacial Maximum and its subsequent retreat history: A review, *Quat. Sci. Rev.*, *21*(1–3), 49–70, doi:10.1016/S0277-3791(01)00083-X.

Årthun, M., K. W. Nicholls, and L. Boehme (2012), Wintertime Water Mass Modification near an Antarctic Ice Front, *J. Phys. Oceanogr.*, *43*(2), 359–365, doi:10.1175/JPO-D-12-0186.1.

Ballentine, C. J., and C. M. Hall (1999), Determining paleotemperature and other variables by using an error-weighted, nonlinear inversion of noble gas concentrations in water, *Geochim. Cosmochim. Acta*, *63*(16), 2315–2336, doi:10.1016/S0016-7037(99)00131-3.

Bayer, P. S. P. R., A. Foldvik, T. Gammelsrod, G. Rohardt, and K. O. M''unnich (1990), Oxygen 18 and helium as tracers of Ice Shelf Water and water/ice interact in the Weddell Sea, *J. Geophys. Res.*, *95*(C3), 3253–3263, doi:10.1029/JC095iC03p03253.

Bender, M., S. Kinter, N. Cassar, and R. Wanninkhof (2011), Evaluating gas transfer velocity parameterizations using upper ocean radon distributions, *J. Geophys. Res.*, *116*, C02010, doi:10.1029/2009JC005805.

Bombosch, A., and A. Jenkins (1995), Modeling the formation and deposition of frazil ice beneath Filchner-Ronne ice shelf, *J. Geophys. Res.*, *100*(C4), 6983–6992, doi:10.1029/94JC03224.

Bromwich, D. H., and D. D. Kurtz (1984), Katabatic wind forcing of the Terra Nova Bay polynya, *J. Geophys. Res.*, *89*(C3), 3561–3572, doi:10.1029/JC089iC03p03561.

Brown, P. J., M. P. Meredith, L. Jullion, A. Naveira Garabato, S. Torres-Valdés, P. Holland, M. J. Leng, and H. Venables (2014), Freshwater fluxes in the Weddell Gyre: Results from $\delta 18O$, *Philos. Trans. R. Soc. A*, *372*(2019), doi:10.1098/rsta.2013.0298.

Burke, A., A. L. Stewart, J. F. Adkins, R. Ferrari, M. F. Jansen, and A. F. Thompson (2015), The glacial mid-depth radiocarbon bulge and its implications for the overturning circulation, *Paleoceanography*, *30*, 1021–1039, doi:10.1002/2015PA002778.

Cheon, W. G., S.-K. Lee, A. L. Gordon, Y. Liu, C.-B. Cho, and J. J. Park (2015), Replicating the 1970s' Weddell Polynya using a coupled ocean-sea ice model with reanalysis surface flux fields, *Geophys. Res. Lett.*, *42*, 5411–5418, doi:10.1002/2015GL064364.

Cox, G. F. N., and W. F. Weeks (1983), Equations for determining the gas and brine volumes in sea-ice samples, *J. Glaciol.*, *29*, 306–316.

de Lavergne, C., J. B. Palter, E. D. Galbraith, R. Bernardello, and I. Marinov (2014), Cessation of deep convection in the open Southern Ocean under anthropogenic climate change, *Nat. Clim. Change*, *4*(4), 278–282.

Eicken, H. (2003), Growth, microstructure and properties of sea ice, in *Sea Ice*: *An Introduction to its Physics, Chemistry, Biology and Geology*, edited by D. N. Thomas and G. S. Dieckmann, Blackwell, Malden.

Emerson, S., T. Ito, and R. C. Hamme (2012), Argon supersaturation indicates low decadal-scale vertical mixing in the ocean thermocline, *Geophys. Res. Lett.*, *39*, L18610, doi:10.1029/2012GL053054.

Foldvik, A., T. Gammelsrød, S. Østerhus, E. Fahrbach, G. Rohardt, M. Schröder, K. W. Nicholls, L. Padman, and R. A. Woodgate (2004), Ice shelf water overflow and bottom water formation in the southern Weddell Sea, *J. Geophys. Res.*, *109*, C02015, doi:10.1029/2003JC002008.

Garabato, A. C. N., D. P. Stevens, A. J. Watson, and W. Roether (2007), Short-circuiting of the overturning circulation in the Antarctic Circumpolar Current, *Nature*, *447*, 194–197, doi:10.1038/nature05832.

Garbe, C. S., U. Schimpf, and B. Jahne (2004), A surface renewal model to analyze infrared images sequences of the ocean surface for the study of air-sea heat and gas exchange, *J. Geophys. Res.*, *109*, C08S15, doi:10.1029/2003JC001802.

Gruber, N. et al. (2009), Oceanic sources, sinks, and transport of atmospheric CO2, *Global Biogeochem. Cycles*, *23*, GB1005, doi:10.1029/2008GB003349.

Hain, M. P., D. M. Sigman, and G. H. Haug (2010), Carbon dioxide effects of Antarctic stratification, North Atlantic Intermediate Water formation, and subantarctic nutrient drawdown during the last ice age: Diagnosis and synthesis in a geochemical box model, *Global Biogeochem. Cycles*, *24*, GB4023, doi:10.1029/2010GB003790.

Hamme, R. C., and S. R. Emerson (2002), Mechanisms controlling the global oceanic distribution of the inert gases argon, nitrogen and neon, *Geophys. Res. Lett.*, *29*(23), 2120, doi:10.1029/2002GL015273.

Hamme, R. C., and S. R. Emerson (2004), The solubility of neon, nitrogen and argon in distilled water and seawater, *Deep Sea Res., Part I*, *51*, 1517–1528.

Hamme, R. C., and J. P. Severinghaus (2007), Trace gas disequilibria during deep-water formation, *Deep Sea Res., Part I*, *54*, 939–950.

Hellmer, H. H. (2004), Impact of Antarctic ice shelf basal melting on sea ice and deep ocean properties, *Geophys. Res. Lett.*, *31*, L10307, doi:10.1029/2004GL019506.

Hohmann, R., P. Schlosser, S. Jacobs, A. Ludin, and R. Weppernig (2002), Excess helium and neon in the southeast Pacific: Tracers for glacial meltwater, *J. Geophys. Res.*, *107*(C11), 3198, doi:10.1029/2000JC000378.

Holland, P. R., A. Jenkins, and D. M. Holland (2008), The Response of Ice Shelf Basal Melting to Variations in Ocean Temperature, *J. Clim.*, *21*(11), 2558–2572, doi:10.1175/2007JCLI1909.1.

Hoppema, M., O. Klatt, W. Roether, E. Fahrbach, K. Bulsiewicz, C. Rodehacke, and G. Rohardt (2001), Prominent renewal of Weddell Sea Deep Water from a remote source, *J. Mar. Res.*, *59*(2), 257–279, doi:10.1357/002224001762882655.

Ito, T., and M. J. Follows (2013), Air-sea disequilibrium of carbon dioxide enhances the biological carbon sequestration in the Southern Ocean, *Global Biogeochem. Cycles*, *27*, 1129–1138, doi:10.1002/2013GB004682.

Ito, T., J. Marshall, and M. Follows (2004), What controls the uptake of transient tracers in the Southern Ocean?, *Global Biogeochem. Cycles*, *18*, GB2021, doi:10.1029/2003GB002103.

Jacobs, S. S. (2004), Bottom water production and its links with the thermohaline circulation, *Antarct. Sci.*, *16*(4), 427–437, doi:10.1017/S095410200400224X.

Jenkins, A., and S. Jacobs (2008), Circulation and melting beneath George VI Ice Shelf, Antarctica, *J Geophys Res*, *113*, C04013, doi:10.1029/2007JC004449.

Jenkins, W. J., D. E. Lott III, B. E. Longworth, J. M. Curtice, and K. L. Cahill (2015), The distributions of helium isotopes and tritium along the U.S. GEOTRACES North Atlantic sections (GEOTRACES GAO3), *Deep Sea Res., Part II*, *116*, 21–28, doi:10.1016/j.dsr2.2014.11.017.

Jullion, L., et al. (2014), The contribution of the Weddell Gyre to the lower limb of the global overturning circulation, *J. Geophys. Res. Oceans*, *119*, 3357–3377, doi:10.1002/2013JC009725.

Karstensen, J., and M. Tomczak (1998), Age determination of mixed water masses using CFC and oxygen data, *J. Geophys. Res.*, *103*(C9), 18,599–18,609, doi:10.1029/98JC00889.

Killawee, J. A., I. J. Fairchild, J.-L. Tison, L. Janssens, and R. Lorrain (1998), Segregation of solutes and gases in experimental freezing of dilute solutions: Implications for natural glacial systems, *Geochim. Cosmochim. Acta*, *62*, 3637–3655.

Le Quéré, C., et al. (2007), Saturation of the Southern Ocean CO$_2$ sink due to recent climate change, *Science*, *316*, 1735–1736.

Liang, J.-H., C. Deutsch, J. C. McWilliams, B. Baschek, P. P. Sullivan, and D. Chiba (2013), Parameterizing bubble-mediated air-sea gas exchange and its effect on ocean ventilation, *Global Biogeochem. Cycles*, *27*, 894–905, doi:10.1002/gbc.20080.

Loose, B., and W. J. Jenkins (2014), The five stable noble gases are sensitive unambiguous tracers of glacial meltwater: Loose and Jenkins; noble gases are tracers of meltwater, *Geophys. Res. Lett.*, *41*, 2835–2841, doi:10.1002/2013GL058804.

Loose, B., P. Schlosser, W. M. Smethie, and S. Jacobs (2009a), An optimized estimate of glacial melt from the Ross Ice Shelf using noble gases, stable isotopes, and CFC transient tracers, *J. Geophys. Res.*, *114*, C08007, doi:10.1029/2008JC005048.

Loose, B., W. R. McGillis, P. Schlosser, D. Perovich, and T. Takahashi (2009b), The effects of freezing, growth and ice cover on gas transport processes in laboratory seawater experiments, *Geophys. Res. Lett.*, *36*, L05603, doi:10.1029/2008GL036318.

Loose, B., W. R. McGillis, D. Perovich, C. J. Zappa, and P. Schlosser (2014), A parameter model of gas exchange for the seasonal sea ice zone, *Ocean Sci.*, *10*, 17–28, doi:10.5194/os-10-17-2014.

Lott, D. E. (2001), Improvements in noble gas separation methodology: A nude cryogenic trap, *Geochem. Geophys. Geosyst.*, *2*(12), 1068, doi:10.1029/2001GC000202.

Lovely, A., B. Loose, P. Schlosser, W. McGillis, C. Zappa, D. Perovich, S. Brown, T. Morell, D. Hsueh, and R. Friedrich (2015), The Gas Transfer through Polar Sea ice experiment: Insights into the rates and pathways that determine geochemical fluxes, *J. Geophys. Res. Oceans*, *120*, 8177–8194, doi:10.1002/2014JC010607.

Lupton, R. A., and H. Craig (1981), A major 3He source at 15°S on the East Pacific Rise, *Science*, *214*, 13–18, doi:10.1126/science.214.4516.13.

Malone, J. L., M. C. Castro, C. M. Hall, P. T. Doran, F. Kenig, and C. P. McKay (2010), New insights into the origin and evolution of Lake Vida, McMurdo Dry Valleys, Antarctica: A noble gas study in ice and brines, *Earth Planet. Sci. Lett.*, *289*(1–2), 112–122, doi:10.1016/j.epsl.2009.10.034.

Marinov, I., A. Gnanadesikan, J. R. Toggweiler, and J. L. Sarmiento (2006), The Southern Ocean biogeochemical divide, *Nature*, *441*, 964–967.

Martinierie, P., D. Raynaud, D. M. Etheridge, J.-M. Barnol, and D. Mazaudier (1992), Physical and climatic parameters which influence the air content in polar ice, *Earth Planet. Sci. Lett.*, *112*, 1–13.

Meredith, M. P. (2013), Oceanography: Replenishing the abyss, *Nat. Geosci.*, *6*(3), 166–167, doi:10.1038/ngeo1743.

Meredith, M. P., A. L. Gordon, A. C. Naveira Garabato, E. P. Abrahamsen, B. A. Huber, L. Jullion, and H. J. Venables (2011), Synchronous intensification and warming of Antarctic Bottom Water outflow from the Weddell Gyre, *Geophys. Res. Lett.*, *38*, L03603, doi:10.1029/2010GL046265.

Mooney, C. Z.; D. (1993), *Bootstrapping: A Nonparametric Approach to Statistical Inference* (*Quantitative Applications in the Social Sciences*), *Sage Univ. Pap. Ser.*, *07*-095.

Namiot, A. Y., and E. B. Bukhgalter (1965), Clathrates formed by gases in ice, *J. Struct. Chem.*, *6*, 873–874.

Naveira Garabato, A. C., A. P. Williams, and S. Bacon (2014), The three-dimensional overturning circulation of the Southern Ocean during the WOCE era, *Prog. Oceanogr.*, *120*, 41–78, doi:10.1016/j.pocean.2013.07.018.

Nicholson, D., S. Emerson, N. Caillon, J. Jouzel, and R. C. Hamme (2010), Constraining ventilation during deepwater formation using deep ocean measurements of the dissolved gas ratios 40Ar/36Ar, N2/Ar, and Kr/Ar, *J. Geophys. Res.*, *115*, C11015, doi:10.1029/2010JC006152.

Notz, D., and M. G. Worster (2009), Desalination processes of sea ice revisited, *J. Geophys. Res.*, *114*, C05006, doi:10.1029/2008JC004885.

Oerter, H., J. Kipfstuhl, J. Determann, H. Miller, D. Wagenbach, A. Minikin, and W. Graft (1992), Evidence for basal marine ice in the Filchner-Ronne ice shelf, *Nature*, *358*(6385), 399–401, doi:10.1038/358399a0.

Ohshima, K. I. et al. (2013), Antarctic bottom water production by intense sea-ice formation in the Cape Darnley polynya, *Nat. Geosci.*, *6*(3), 235–240, doi:10.1038/ngeo1738.

Orsi, A. H., W. M. J. Smethie, and J. L. Bullister (2002), On the total input of Antarctic waters to the deep ocean: A preliminary estimate from chlorofluorocarbon measurements, *J. Geophys. Res.*, *107*(C8), 3122, doi:10.1029/2001JC000976.

Poole, R., and M. Tomczak (1999), Optimum multiparameter analysis of the water mass structure in the Atlantic Ocean thermocline, *Deep Sea Res., Part I*, *46*, 1895–1921.

Schlosser, P., R. Bayer, A. Foldvik, T. Gammelsröd, G. Rohardt, and O. K. Münnich (1990), Oxygen 18 and Helium as tracers of ice shelf water and water/ice interaction in the Weddell Sea, *J. Geophys. Res.*, *95*(C3), 3253–3263, *doi*:10.1029/JC095iC03p03253.

Sievers, H. A., and W. D. Nowlin (1984), The stratification and water masses at Drake Passage, *J. Geophys. Res.*, *89*(C6), 10,489–10,514, doi: 10.1029/JC089iC06p10489.

Sigman, D. M., M. P. Hain, and G. H. Haug (2010), The polar ocean and glacial cycles in atmospheric CO2 concentration, *Nature*, *466*(7302), 47–55, doi:10.1038/nature09149.

Stanley, R. H. R., W. J. Jenkins, and S. C. Doney (2006), Quantifying seasonal air-sea gas exchange processes using noble gas time-series: A design experiment, *J. Mar. Res.*, *64*, 267–295.

Stanley, R. H. R., G. Baschek, D. E. I. Lott, and W. J. Jenkins (2009a), A method for measuring noble gases and their isotopic ratios using programmed multistage cryogenic trapping and a combination of quadrupole and magnetic sector mass spectrometers, *Geochem. Geophys. Geosystems*, *10*, Q05008, doi:10.1029/2009GC002429.

Stanley, R. H. R., B. Baschek, D. E. Lott, and W. J. Jenkins (2009b), A new automated method for measuring noble gases and their isotopic ratios in water samples, *Geochem. Geophys. Geosystems*, *10*, Q05008, doi:10.1029/2009GC002429.

Stanley, R. H. R., W. J. Jenkins, D. E. I. Lott, and S. C. Doney (2009c), Noble gas constraints on air-sea gas exchange and bubble fluxes., *J. Geophys. Res.*, *114*, C11020, doi:10.1029/2009JC005396.

Stephens, B. B., and R. F. Keeling (2000), The influence of Antarctic sea ice on glacial-interglacial CO_2 variations, *Nature*, *404*, 171–174.

Stute, M., and P. Schlosser (1993), Principles and Applications of the Noble Gas Paleothermometer, in *Climate Change in Continental Isotopic Records*, edited by P. K. Swart, et al., pp. 89–100, AGU, Washington, D. C.

Stute, M., and P. Schlosser (2000), Atmospheric noble gases, in *Environmental Tracers in Subsurface Hydrology*, edited by P. G. Cook and A. L. Herczeg, pp. 349–377, Springer, Boston, Mass.

Stute, M., M. Forster, H. Frischkorn, A. Serejo, and J. F. Clark (1995), Cooling of tropical Brazil (5°C) during the Last Glacial Maximum, *Science*, *269*, 379–383.

Talley, L. D. (2008), Freshwater transport estimates and the global overturning circulation: Shallow, deep and throughflow components, *Prog. Oceanogr.*, *78*(4), 257–303, doi:10.1016/j.pocean.2008.05.001.

Toggweiler, J. R. (1999), Variation of atmospheric CO_2 by ventilation of the ocean's deepest water, *Paleoceanography*, *14*(5), 572–588, doi: 10.1029/1999PA900033.

Tomczak, M. (1981), A multiparameter extension of temperature/salinity diagram techniques for the analysis of non-isopycnal mixing, *Prog. Oceanogr.*, *10*, 147–171.

Top, Z., S. Martin, and P. Becker (1988), A laboratory study of dissolved noble gas anomaly due to ice formation, *Geophys. Res. Lett.*, *15*(8), 796–799, doi:10.1029/GL015i008p00796.

Wanninkhof, R. (1992), Relationship between Wind-Speed and Gas-Exchange over the Ocean, *J. Geophys. Res.*, *97*(C5), 7373–7382, doi: 10.1029/92JC00188.

Weiss, R. F. (1971), Solubility of helium and neon in water and seawater, *J. Chem. Eng. Data*, *16*, 235–240.

Weiss, R. F., and T. K. Kyser (1978), Solubility of krypton in water and sea water, *J. Chem. Eng. Data*, *23*(1), 69–72, doi:10.1021/je60076a014.

Well, R., W. Roether, and D. P. Stevens (2003), An additional deep-water mass in Drake Passage as revealed by [3]He data, *Deep Sea Res., Part I*, *50*, 1079–1098.

Wood, D., and R. Caputi (1966), *Solubilities of Kr and Xe in Fresh and Sea Water*, U.S. Nav. Radiol. Def. Lab., San Francisco, Calif.